Seismic Monitoring of Permafrost in Svalbard, Arctic Norway

Albaric, Julie

2021-09

Albaric , J , Kuhn , D , Ohrnberger , M , Langet , N , Harris , D , Polom , U , Lecomte , I &
Hillers , G 2021 , ' Seismic Monitoring of Permafrost in Svalbard, Arctic Norway ' ,
Seismological Research Letters , vol. 92 , no. 5 , pp. 2891-2904 . https://doi.org/10.1785/0220200470

http://hdl.handle.net/10138/345952
https://doi.org/10.1785/0220200470

unspecified
acceptedVersion

Seismic monitoring of permafrost in Svalbard, Arctic Norway

J. Albaric[1*] D. Kühn[2] M. Ohrnberger[3] N. Langet[2]

D. Harris[4] U. Polom[5] I. Lecomte[6,2] G. Hillers[7]

[1] Chrono-environnement, University of Franche-Comté, Besançon, France

[2] Applied Seismology, NORSAR, Kjeller, Norway

[3] Institute of Geosciences, University of Potsdam, Germany

[4] Deschutes Signal Processing LLC, Maupin, Oregon, USA

[5] Leibniz Institute for Applied Physics, Hannover, Germany

[6] Department of Earth Science, University of Bergen, Bergen, Norway

[7] Institute of Seismology, University of Helsinki, Helsinki, Finland

November 22, 2021

The authors acknowledge there are no conflicts of interest recorded.

*corresponding author: julie.albaric@univ-fcomte.fr; formerly at: Applied Seismology, NORSAR, Kjeller, Norway

Abstract

We analyze data from passive and active seismic experiments conducted in the Adventdalen valley of Svalbard, Norwegian Arctic. Our objective is to characterize the ambient wavefield of the region and to investigate permafrost dynamics through estimates of seismic velocity variations. We are motivated by a need for early geophysical detection of potentially dangerous changes to permafrost stability. We draw upon several data sources to constrain various aspects of seismic wave propagation in the Adventdalen. We use $f-k$ analysis of five years of continuous data from the SPITS array to demonstrate that ambient seismic noise on Svalbard consists of continuously-present body waves and intermittent surface waves appearing at regular intervals. A change in wavefield direction accompanies the sudden onset of surface waves, when the average temperature rises above the freezing point, suggesting a cryogenic origin. This hypothesis is supported further by our analysis of records from a temporary broadband network, which indicates that the background is dominated by icequakes. Synthetic Green's functions calculated from a 3-D velocity model matched well with empirical Green's functions constructed from the recorded ambient seismic noise. We use a shallow shear wave velocity model, obtained from active seismic measurements, to estimate the maximum depth of Rayleigh wave sensitivity to changes in shear velocity to be in the 50 to 100 meters range. We extract seasonal variations in seismic velocities from ambient noise cross-correlation functions computed over three years of SPITS data. We attribute relative velocity variations to changes in the ice content of the shallow (2-4 meter depth) permafrost, which is sensitive to seasonal temperature changes. A linear decreasing trend in seismic velocity is observed over the years, most likely due to permafrost warming.

Keywords— Permafrost , environmental seismology, ambient seismic noise, seismic velocity change, icequakes, climate change, Arctic, $f-k$ analysis, shear wave active seismic experiment

Introduction

Warming of permafrost in polar territories is a major concern associated with the overall change of the global climate system, especially because of its potential for greenhouse gases emission (Anisimov, 2007; Schaefer et al., 2014). Monitoring its dynamic properties is thus essential. Permafrost is thermally defined as ground that remains at or below 0°C for at least two consecutive years (Williams and Smith, 1989). The top of the permafrost, called the active layer, is subject to summer thawing and winter freezing. Below, the permafrost shows seasonal subzero temperature variations down to the depth of zero annual amplitude (e.g., Isaksen et al., 2007). Pore-space of permafrost can be filled with a variable proportion of gas, ice and water, depending on several factors such as temperature, pore size and shape, nature of the water, salinity and stress state (e.g., Timur, 1968; Zimmerman and Michael, 1986; Stemland et al., 2020).

Seismic monitoring is one of the most suitable methods for detecting changes in permafrost dynamic properties, as seismic velocities are particularly sensitive to the ice content of the ground, that increase for example when water in the pore medium is freezing (e.g., Timur, 1968; Zimmerman and Michael, 1986; LeBlanc et al., 2004; Dou and Ajo-Franklin, 2014; Dou et al., 2016; Stemland et al., 2020). As temperature decreases below 0°C, interstitial water freezes, first within larger pore spaces, then within smaller ones, resulting in a gradual increase in seismic velocities (Timur, 1968; Zimmerman and Michael, 1986; LeBlanc et al., 2004). This phenomenon has been observed in the active layer by several studies analyzing seasonal velocity change based on ambient seismic noise monitoring (James et al., 2017, 2019; Kula et al., 2018; Köhler and Weidle, 2019) and repeated active seismic experiments (Stemland et al., 2020). In addition, velocity contrasts associated with unfrozen interstitial water were detected below the active layer, in particular through P- and S- wave seismic tomography (LeBlanc et al., 2004) and active surface wave surveys (Dou and Ajo-Franklin, 2014). For example, the laboratory analysis from Zimmerman and Michael (1986) indicated an increase of P- and S- wave velocity of more than 10% in some permafrost sediment core samples due to ice saturation increase between -5°C and -15°C.

In this paper, we investigate changes in the properties of permafrost related to seasonal temperature changes. We estimate seismic velocity variations using three years of ambient seismic noise recorded on Svalbard, Norway (Fig. 1). The Svalbard archipelago is located in the Arctic Ocean on the northwestern margin of the Barents Sea shelf (e.g., Bungum et al., 1991). The area exhibits regular seismic activity comprising tectonic and glacial events (e.g., Köhler et al., 2012; Pirli et al., 2013). Our research concentrates on the Adventdalen valley close to the town of Longyearbyen, located on Spitsbergen island. The geological and tectonic characteristics of Adventdalen were studied in detail, in particular in association with the carbon capture and storage (CCS) research carried out by the Longyearbyen CO_2 Lab of the University Centre in Svalbard (UNIS; Braathen et al., 2012; Senger et al., 2014; Olaussen et al., 2019). Drill cores at the location of the CO_2 Lab indicated 60-70 m of Holocene gravel and sand followed by a succession of sandstones, silts and shales comprising the Cretaceous formations of the Adventalen group overlying a sandstone unit targeted as a potential CO_2 reservoir at ∼670 m depth. Microseismic monitoring at the CO_2 Lab was described in Oye et al. (2010, 2013), Kühn et al. (2014) and Harris et al. (2017).

Permafrost on Spitsbergen is overlain by a seasonally unfrozen active layer of about 0.8 to ∼2 m thickness, and underlies at least 90% of the land surface not covered by glaciers (Humlum et al., 2003; Christiansen et al., 2010; Westermann et al., 2010). The total permafrost thickness was estimated to be 120-160 m at the CO_2 Lab (Braathen et al., 2012) and 220 m within the Janssonhaugen temperature borehole (JB in Fig. 1; Isaksen et al., 2001). Permafrost warming on Svalbard was already detected and will likely continue over the next century (Isaksen et al., 2007; Seneviratne et al., 2016).

Thus, seismic monitoring of permafrost resilience or vulnerability, respectively, is both vital and crucial.

The analysis of Green's functions (or cross-correlation functions, CCFs) constructed from the ambient wavefield through seismic interferometry (e.g., Shapiro and Campillo, 2004; Snieder, 2004; Hadziioannou et al., 2009) has become a standard tool in seismology for imaging (e.g., Shapiro et al., 2005; Roux et al., 2011; Lehujeur et al., 2018) and monitoring temporal changes in seismic velocity (e.g., Snieder et al., 2002; Sens-Schönfelder and Wegler, 2006; Brenguier et al., 2008; Hillers et al., 2015). Techniques measuring interstation noise correlation functions allow to track variations in propagation characteristics over time and distance scales governed by the coherent parts of the ambient wavefield.

We processed seismic data from passive and active monitoring systems (Fig. 1): a permanent small-aperture array (SPITS), a local temporary network (SEISVAL) and an active S-wave seismic experiment at the CO_2 Lab. The results of the active seismic experiment allowed improved estimates of the shallow velocity structure of Adventdalen and served for event location and Rayleigh wave sensitivity analysis. SPITS and SEISVAL seismic recordings were both used to characterize the ambient wavefield. SEISVAL CCFs were compared with synthetics computed through a large-scale 3D velocity model of the Adventdalen to improve our interpretation of scattered wave propagation in the valley. From the SPITS CCFs, we estimated long-term seasonal velocity variations in the permafrost.

Seismic monitoring networks in Adventdalen

Permanent seismic array: SPITS

The SPITS array (Fig. 1) is located about 10 km south-east of Longyearbyen on an outcrop of the Helvetiafjellet geological formation, consisting of sandstone, shale, coal and conglomerate. It was installed by NORSAR in 1992 (Mykkeltveit et al., 1992) for seismic monitoring of the archipelago and the Arctic, and is today part of the Comprehensive Nuclear-Test-Ban Treaty (CTBT) international monitoring system (Schweitzer et al., 2021). This permanent installation currently consists of 9 broadband stations arranged on two concentric circles with 500 m and 1 km diameter, respectively (Guralp CMG-3TB, 100 s-50 Hz, connected to CMG-DM24 digitizers; Pirli, 2003). Stations record data continuously at 80 Hz on 3 components, except for three 1-component stations (SPA1, SPA2 and SPA3; Fig. 1). The sensors are installed at 6 m depth to be shielded from noise produced by wind and anthropogenic activities. The data are automatically and manually processed by NORSAR for earthquake bulletins (NORSAR, 1971) distributed to national and international data centres.

Temporary broadband network: SEISVAL

The SEISVAL temporary network (Fig. 1) consisted of 12 stations deployed in Adventdalen during summer 2014 (May to September). Six of the sensors were CMG 40 instruments (Guralp, 60 s-50 Hz), the remaining six were

Noemax seismometers (Agecodagis, 20 s-50 Hz). The sampling frequency of the Taurus digitizers was set to 100 Hz. Most of the stations were installed on large blocks of rock, in some cases requiring an additional cement base to enhance leveling, in particular for the Noemax sensors. Two stations (STN07 and STN08) were installed on existing concrete bases and one (STN12) inside a cabin. Each sensor was protected with a plastic box insulated with rock wool and sealed to the rock with cement. Most of the stations acquired data during the whole installation period; however, station STN04 stopped recording in mid-June, station STN08 from mid-July to mid-August, and station STN10 did not record data except for a very short period. From spectrograms, it was evident that STN01 was malfunctioning at least during the last period of the deployment.

Active seismic experiment

S-wave reflection and vibroseis downhole experiments

To build a 1-D velocity model of the shallow subsurface, vibroseis S-wave reflection and downhole experiments were conducted in September 2012 (Oye et al., 2013).

For the S-wave reflection experiment, a 100 m long profile was acquired on a gravel road in the Longyearbyen CO_2 Lab area (see CO_2 Lab marker on Fig. 1 and P2 seismic line on Fig. S1). The S-wave source consisted of an electro-dynamically driven linear shaker (ELVIS micro-vibrator) mounted below a wheelbarrow frame (Polom, 2006; Polom et al., 2010, 2011) utilizing the Vibroseis method (Crawford et al., 1960). The shaking orientation was perpendicular to the acquisition line to generate horizontally polarized S-waves (SH). The signals were recorded by 48 horizontal geophones (SH-mode, SM6-H 10 Hz) mounted every 2 m on a land-streamer. Data were pre-processed using the VISTA 10.028 seismic data processing software (GEDCO Inc., Calgary, CA). The shallowest ten metres of the profiles were affected by the presence of the road inducing an artificial velocity layer and thus, were removed from the analysis. Fig. 2a depicts a sequence of 2-fold stacked raw records from P2, acquired on the main road. FX-deconvolution was applied to reduce wind noise before finite-difference time migration using smoothed stacking velocities. S-wave interval velocities derived from the stacking velocities are presented together with the depth-converted final section in Fig. 2b. The results indicated low S-wave velocities of about $\sim$200 m/s in the upper 50 m, increasing to $\sim$450 m/s at 75 m depth. Due to the limited acquisition line spread of 95 m and wind noise affecting the raw data, the precision of velocity calculation decreased at greater depth and could not be interpreted.

A complementary S-wave vibroseis downhole experiment was carried out around observation well Dh3 (Fig. S1b). Dh3 was equipped with a string of five 3-component geophones located between 94 and 294 m depth with 50 m spacing. The string was connected to a Geometrics GEODE automatic recording system used for continuous passive seismic monitoring (Kühn et al., 2014). The ELVIS micro-vibrator was employed again to generate SH and SV polarised shear waves at shot points around the well (S1 to S11 on Fig. S1). Data processing included adjusting the source timing, a static shift, a vibroseis correlation (Crawford et al., 1960), bandpass filtering between 20 and 85 Hz, and normalising the traces. The processed data are presented in the supplementary material (Fig. S2). Results were similar for both SV and SH source configurations. P-wave arrivals could be identified on the vertical components down to the 194 m depth level. Since the S-wave onset was visible only at 94 m depth, the S-wave arrival was determined by waveform matching on the other geophones. Accordingly, P- and S-wave velocities were well resolved down to 194 m depth. The average P-wave velocity from the surface to 94 m depth was 1800 m/s (505 m/s for the S-wave velocity) and 3571 m/s between 94 and 194 m depth (1726 m/s for the S-wave velocity).

Velocity model building

To construct a near-surface 1-D velocity model, results from both the reflection and vibroseis downhole experiments were integrated (Fig. S3a,b). For the S-wave model, velocities from the reflection experiment from the surface to 75 m depth were combined with the velocities extracted from the vibroseis downhole survey for depths between 94 and 194 m. Velocities were linearly interpolated between 75 and 94 m depth. However, the S-wave velocities in the uppermost part of the velocity model may still be overestimated due to the presence of a gravel road. The P-wave velocity model was less well constrained and a value of 1500 m/s was assumed at the surface following

Bælum et al. (2012). The velocity at 75 m depth was derived from the S-wave velocity employing a Vp/Vs ratio of 1.7. For the depth range between 94 and 194 m, the P-wave velocity model was based on the downhole experiment results (Figs. S2, S3b).

Within the scope of the Longyearbyen CO_2 Lab project, active seismic experiments were conducted to assess the potential for CO_2 sequestration and to develop a 3-D reservoir model for the Adventdalen valley (Bælum et al., 2012; Braathen et al., 2012; Senger et al., 2014). From these measurements, recorded by snow streamer in winter conditions, only P-waves velocities were available focusing on the bedrock succession, especially the proposed reservoir layer. The main feature of the reservoir model was strata dipping towards the southwest by 1-3°, such that the proposed reservoir layer, situated at 670-970 m depth below the CO_2 Lab, outcropped 15-20 km to the northeast (Bergh et al., 1997; Braathen et al., 2012). From this model, a 3-D raytracing model was constructed (see Fig. 7 in Lubrano Lavadera et al., 2018). We employed this model for the computation of synthetic Green's functions to resolve potential 3-D effects, for example caused by topography (section *Modelling cross-correlation functions*). The near-surface 1-D velocity model was extended to larger depths by merging it with a profile from the 3-D raytracing model extracted at the CO_2 Lab location (Fig. S3c,d). We used this composite 1-D velocity model as described in the following sections to locate the microseismic events recorded on the temporary broadband network (section *Local microseismicity and icequakes*) and to analyze the influence of S-wave velocities on the Rayleigh-wave velocity (section *Rayleigh wave sensitivity*).

Characterisation of the ambient wavefield

Local microseismicity and icequakes

This section assesses the contribution of microseimicity and icequake activity to the ambient wavefield in Adventdalen. In particular, we investigated the benefit of installing the SEISVAL temporary network to enhance the detection capacity for local events. Because of the small aperture of the SPITS array, only the central station (SPA0) was included in the analysis. The event detection was carried out manually, by visually screening 30-minute-long signals recorded at all stations and components between May and September 2014. It resulted in the selection of about 1000 potential seismic event records. In a second step, regional events reported by the NORSAR reviewed bulletin (magnitude ≥ 2.0) or unsupervised GBF (Generalized Beamforming) bulletin (NORSAR, 1971) were rejected, leaving 250 potential local events.

Three event types were observed: (1) short-duration signals characterized by distinct P- and S-wave arrivals associated with local events (Fig. 3 a,b), (2) longer-duration signals distinguished by two distinct phases with a temporal separation on the order of 10 s associated with regional events not reported in the previous catalogues (Fig. 3c), and (3) long-duration signals (> 100 s or more) associated with source processes that were more difficult to identify and were therefore classified as noise. The first two categories of events were located employing the 1-D velocity model extended to larger depths (Fig. S2c,d) and a grid-search. They appeared to occur mainly in two areas to the southeast and north of the network, co-located with a coal mine and glaciers (Fig. 1). Using waveform cross-correlation, events were classified into clusters, among which the events to the southeast and north represent two well-correlated families. However, the P-wave arrivals of the events located to the southeast in the vicinity of the mine contained more energy at higher frequencies ($\leq$10 Hz; Fig. S4). We noted further that the events located close to the mine were distributed randomly in time, whereas the events located in the north occurred within 15 days in July 2014.

Previous studies of icequakes in Svalbard (e.g., Köhler et al., 2012, 2015) observed a wide variety of seismic signals associated with glaciers. Therefore, while the events to the north can be interpreted as icequakes, we cannot conclusively determine if the seismicity to the southeast represents mining-induced events or icequakes.

Spectral and $f-k$ analyses of the ambient seismic noise

In order to characterize the spectral content of the ambient seismic wavefield, we analyzed data recorded by the SPITS array from 2007 to 2014 in the frequency range between 0.1 and 40 Hz. In a first step, probabilistic power spectral density functions (PPSDs, McNamara et al., 2009) were computed to establish ambient seismic noise baselines: long-term yearly baselines to characterize ambient noise conditions and short-term weekly as well as monthly baselines to determine changing station performance and noise characteristics (Fig. S5). At frequencies below 0.2 Hz and above 5 Hz, the ambient seismic noise was close to the new low noise model (Petersen, 1993). The maximum energy was present at about 0.2-0.3 Hz, corresponding to the secondary microseism. A stable source of noise was also recovered at 0.5-4 Hz. In addition, seasonal changes occurred in the noise level. At high frequencies (> 2 Hz), the level of noise was higher in summer than in winter, which can be explained by the increase in icequake activity due to ice melting (Köhler et al., 2015). On the contrary, low frequency noise was stronger in winter, most likely due to the dynamic weather conditions similar to those described for Norway (Demuth et al., 2016) or to the strong noise source in the northern Atlantic Ocean dominating during winter (Stehly et al., 2006).

To better characterize the direction in which ambient seismic noise propagates across the array, a frequency-wavenumber ($f - k$) technique (Kværna and Ringdahl, 1986; Krim and Viberg, 1996; Rost and Thomas, 2002) was applied in the frequency bands 0.5-2 Hz, 1.5-4.5 Hz, 3-9 Hz and 6-18 Hz. Lower frequencies were omitted due to the small aperture of the SPITS array and correspondingly limited resolution. The time resolution of the sliding window analysis was adjusted to capture high frequency transients of both tectonic and cryogenic origin as well as background noise around 1 Hz. For each time window, the following wave-field attributes were recorded: the absolute horizontal slowness, the direction of propagation, the coherency of the wavefield via the multi-trace semblance coefficient (Neidell and Taner, 1971) and the beam power.

The overall output of the analysis windows was summarized with histograms for individual wavefield parameters. To resolve diurnal changes, the summary histograms were computed for 3-hour intervals representing the $f - k$ results from $\sim$ 3600 time windows (lowest frequency band) to $\sim$ 108, 000 time windows (highest frequency band).

Figure 4 shows histograms of absolute horizontal slowness values binned in 0.02 s/km and within 3-hour time windows. For all frequency ranges, the histograms peaked at typical P- and S-wave slownesses of crust and upper mantle. This pattern was a temporally stable feature throughout the years with recurring short-lived interruptions during early summer months when surface wave propagation velocities became dominant. In order to investigate this annual pattern, we filtered the analysis results keeping only time windows showing slownesses in the range from 0.33 s/km to 1 s/km. In Fig. 5, we show the resulting backazimuth distributions of the seasonally dominating surface wavefield (see Fig. S6 for the summer period of 2011). We observed an abrupt change of the backazimuth pattern of the surface wave field in the first days of June. Coinciding with the average air temperature rising above the freezing point, the histograms show strong arrivals at several backazimuths in both northern and southern directions, the most pronounced being N140°E–N160°E. The directional source concentration persisted for a few weeks. After disappearing for two weeks at the end of the summer, two other activity bursts from southeastern directions were detected. This behaviour was visible for all studied years (2010-2013; Fig. 5).

We attribute this consistent seasonal pattern to cryogenic glacier-related seismicity typically being active during summertime, probably due to the effect of increasing temperature promoting cracks within the glacier body and allowing for basal gliding due to melt water accumulating at its base. Köhler et al. (2015) reported the occurrence of such concentrated seismicity in the frequency band from 1 to 8 Hz for a large number of glaciers in Svalbard. In particular, during summers and autumns within the years 2007 to 2013, daily icequake activity was recorded at Kongsfjorden (to the NNW) and Hornsund (to the S). Also the analysis of microseismicity in this study features event locations correlated with glaciers around Adventdalen.

Ambient seismic noise cross-correlation

Cross-correlation functions computation

Data processing was performed using a Python code developed for dense array noise-correlation studies (Boué et al., 2013; Boué et al., 2014). Daily cross-correlation functions (CCFs) were computed separately for the SEISVAL network and the SPITS array.

The SEISVAL network consisted of two different types of sensors, thus the instrument response had to be homogenised first. Since the Guralp CMG40 instrument response features the wider spectrum, the data recorded by these sensors were corrected to the Noemax Agecodagis instruments instead. Because of the different number of components of the SPITS sensors, the analysis of these data focused only on pairs of vertical component.

Data were bandpass-filtered between 0.01 and 30 Hz for SPITS and between 0.03 and 40 Hz for SEISVAL. Daily records were split into 6-hour segments for SPITS and into 2-hour segments for SEISVAL. The mean and the trend of the time series were removed. A data segment was rejected if its elevated relative energy content suggested contamination with an earthquake or icequake signal. Spectral whitening was applied to the segments (50 s to 20 s for SPITS, 25 s to 30 Hz for SEISVAL), followed by time domain clipping at 3.5-times the standard deviation of the amplitude distribution in each time window.

Example normalised daily CCFs are plotted in Fig. 6 for the frequency range of 0.5-2 Hz for the whole year 2011 for SPITS and for days-of-year 127 to 255 of 2014 for SEISVAL. The abscissa denotes lag time and the ordinate calendar time. The stack over all days is presented at the top of the panels.

Compared to the SEISVAL CCFs, the shorter interstation distances at the SPITS array led to higher signal-to-noise ratios and shorter travel times of the main Rayleigh wave arrival around 0 s lag time, and the correlation coda exhibited stable arrivals that were used for velocity change monitoring. The symmetry of the SPITS CCFs tended to vary seasonally, resulting from variations in the noise source directions (Stehly et al., 2006) as illustrated in the previous section.

The CCFs reconstructed between STN02 and STN06 on the north side of Adventdalen contained a signal at positive lag times, while the CCFs between STN07 and STN09 on the south side of Adventdalen featured an arrival at negative lag times. STN06 and STN07 were located to the southeast, whereas STN02 and STN09 were located to the northwest (Fig. 1). The observed asymmetries seem to be a general feature for northwest-southweast oriented travel paths along the northern and southern edge of the Adventdalen valley, suggesting that at least in the analyzed frequency bands, noise sources were spatially heterogeneous and clustered towards the northwest (compare to Fig. 1 in Stehly et al., 2006). For CCF stacks corresponding to travel paths across the valley, the signals were more symmetric compared to the travel paths along the valley. This strongly suggests a predominant energy flux along the valley, which can be explained by the skewed noise source distribution in combination with the topography forming a guide for wave propagation.

Modelling cross-correlation functions

To better understand the cross-correlation function properties, we modelled wave propagation in Adventdalen. For a diffuse equipartitioned noise field, the nine cross-correlations between pairs of seismograph components are empirical estimates of the corresponding Green's functions (Lobkis and Weaver, 2001; Snieder, 2004; Tsai, 2010).

We employed the 3-D velocity model described in section *Velocity model* *building*, combined with a topographic model of the region. The computational domain consisted of a volume of 10 $\times$ 15 $\times$ 3 km^3 covering the locations of the temporary broadband network stations and the CO_2 Lab, with a 3 km margin on all sides to reduce boundary effects. Calculations, carried out using 1,024 processors of a supercomputer, were accurate to 9 Hz. Given the minimum shear wave speed of 660 m/s in the 3-D velocity model, this required a grid spacing of 9 m leading to about 6.2×10^8 grid points and a time step of 0.0012 s/sample for simulation times of 7.5 s. Computations were carried out using the SW4 4$^{\text{th}}$-order accurate finite difference code for seismic wave propagation (Sjögreen and Petersson, 2012; Petersson and Sjögreen, 2015; Petersson and Sjögreen, 2017). We took a reciprocal approach to the calculations (Eisner and Clayton, 2001), placing a source at each station location in turn, while recording at the remaining stations. This entailed three forward runs of the elastic finite-difference model at each of the station locations applying a force in each of the three cartesian directions, recording the 6-component strain tensor at each of the other eleven stations.

Fig. 7 compares the modelled Green's functions with the cross-correlation function stacks for sensor pairs situated on the south side of Adventdalen by taking the derivative of the latter. For the signals at negative time lags, the agreement between measured and modelled Green's functions was remarkable providing an independent validation of the 3-D velocity model. A similarly good match could be observed for sensor pairs along the north side of Adventdalen for positive lag times and for most of the short travel paths across the valley, i.e. for sensor pairs STN06-STN07, STN02-STN09, and STN05-STN08. For the remaining station pairs, especially for the longer propagation paths across the valley, the agreement was less good. A polarisation analysis of the modelled seismograms confirmed the propagating waves as Rayleigh waves.

Seismic velocity variation monitoring

Rayleigh wave sensitivity

We analyzed the sensitivity of Rayleigh waves at depth to changes in shear wave velocity following Boore and Nafi Toksöz (1969). To this end, we computed derivatives of fundamental Rayleigh wave phase and group velocity curves for a large frequency band (0.2 to 20 Hz) in response to changes in S-wave velocity within 100 individual layers of increasing thickness up to the model depth of 1200 m (Fig. 8).

As velocity model, we used the extended 1-D S-wave velocity (Fig. S3c). P-wave and density variations were not considered because the sensitivity of surface wave velocity to P-wave velocity and density variations are small compared to shear wave velocity changes (Boore and Nafi Toksöz, 1969). Domains in the frequency-depth plot for which an increase in shear wave velocity leads to an increase in Rayleigh wave velocities are shown in blue, whereas an anti-correlated response is indicated in red. White regions show neutral response. For this shear wave velocity model, sensitivities of Rayleigh wave phase and group velocities are strongest within the uppermost 100 m. Down to depths of approximately 80 m, where the shear wave velocity increased abruptly, a change of 1 m/s in shear wave velocity caused a change of up to 0.2 m/s in Rayleigh wave velocity (for both phase and group velocities), corresponding to a fractional change of 20 %.

Velocity changes in permafrost at SPITS

We investigated three years of data for evidence of velocity changes in the subsurface using CCFs computed from all vertical components included in the SPITS array. Prior to the analysis, we removed sporadic low-quality correlations from the three-year gathers. Relative travel time changes (dt/t) were estimated in the coda of the CCFs to infer a potential relative velocity variation ($dv/v = -dt/t$; e.g., Snieder et al., 2002; Brenguier et al., 2008; Hadziioannou et al., 2009; Hillers et al., 2015). This analysis is typically performed using the time-domain stretching method (Sens-Schönfelder and Wegler, 2006) or the spectral doublet method (Poupinet et al., 1984), also known as the moving window cross-spectral method (MWCS). Both methods were tested and gave similar results. We continue showing the results from the doublet method.

For each station pair, a reference cross-correlation function (RCCF) was constructed using the stack of all daily CCFs over the study period. Subsequently, a ± 10 days moving-average stack of daily CCFs was compared to this RCCF. The MWCS method was applied to the coda of the CCFs at negative and positive lag times between 8 and 20 s. This window starts sufficiently late in the coda after the arrival of the direct surface wave to minimise the influence of ballistic components or azimuthal variations in the distribution of noise sources (Colombi et al., 2014). The final dv/v estimate was obtained by averaging over all station pairs. We investigated different frequency bands but focus here on the results obtained in the 0.5 to 2 Hz range (Fig. 9). The $f-k$ analysis shows higher plane wave energy arriving at higher frequencies compared to the body wave components or the relative surface wave energy in this frequency range (Fig. 4). However, the cleaner dv/v measurements are obtained in the target range 0.5-2 Hz, which reflects the comparatively higher coherency of the reconstructed coda waves at these longer periods.

Strong seasonal variations in seismic velocity were resolved with a maximum amplitude of about $\pm$ 0.08%, in addition to a linearly decreasing trend (Fig. 9). An anti-correlation between changes in seismic velocity and temperatures measured between 0.5 and 15 m depth in a nearby borehole (Isaksen et al., 2001, 2007) is clearly visible. Once the temperatures increased, seismic velocities decreased and vice-versa. This anti-correlation was particularly in phase with temperature variations at 2-4 m depth (Fig. 9b).

In the JB borehole close to the SPITS array (Fig. 1), the permafrost and active layer thicknesses are 220 m and 1.5-1.7 m, respectively (Isaksen et al., 2007). Below the active layer and down to $\sim$10 m depth, the permafrost experiences seasonal temperature fluctuations below the freezing point (Fig.

9; Isaksen et al., 2007). These seasonal temperature changes influence the ice content of the ground, which significantly affects its seismic properties, in particular the shear modulus (e.g., Timur, 1968; Zimmerman and Michael, 1986; LeBlanc et al., 2004; Dou and Ajo-Franklin, 2014; Dou et al., 2016; James et al., 2017, 2019; Stemland et al., 2020). In Alaska, James et al. (2017) monitored large velocity changes in the active layer employing the MWCS method based on high frequency noise recordings (13-17 Hz), resulting in dv/v values of up to $\sim$10%. The authors pointed out that the measured amplitudes of dv/v were lower than expected for thawing (90%), because only a portion of the wave energy could be recovered.

Ambient seismic noise across the SPITS array exhibited a higher coherency in a lower frequency range compared to the study of James et al. (2017), which allowed us to resolve velocity changes at 0.5-2 Hz. The estimated dv/v amplitude was lower compared to the observations by James et al. (2017) in the active layer. Figure 9 illustrates that the smoothed dv/v estimates are in phase and anti-correlated with the temperature variations at 2-4 m depth. From this, we interpret that the velocity variations observed in the frequency range 0.5 to 2 Hz are governed by temperature changes below the active layer but above the depth of zero annual mean temperature change at $\sim$10 m depth (Fig. 9b). Temperature and thus velocity variations at this depth level may be explained by ice saturation with the percentage of unfrozen interstitial water drastically affecting the permafrost seismic properties (Zimmerman and Michael, 1986; LeBlanc et al., 2004; Dou and

Ajo-Franklin, 2014; Stemland et al., 2020). In particular, the ice saturation is most likely controlled by the degree of salinity of the Adventdalen group geological formation (Stemland et al., 2020). To examine the possibility that spurious dv/v measurements may be caused by systematic temporal changes in the wavefield associated with icequake activity, we compared the temporal distributions of events in the NORSAR $f-k$ analysis (NORSAR, 1971) with the dv/v time series and the temperature variations at 3 m depth (Figure 10).

The rose plots in Fig.10 suggest that most of the detected events are located in N-S direction, consistent with the glacier activity described in the previous section and in Köhler et al. (2015). The majority of events is characterised by a high frequency content: the number of detections decreases by factor 18 between the frequency bands 1-4 Hz and 0.5-2 Hz. In the event count plot, the number of daily detections (normalised over the full three-year period) is color-coded and compared to the dv/v time series filtered in the same frequency bands. In the 1-4 Hz range, a strong increase in the number of events detected during summer is discernible, consistent with an increase in icequake activity. However, significant seasonal dv/v variations are absent. In contrast, the low-frequency results exhibiting the strongest seasonal dv/v variations show much less icequake activity.

These results are thus not implying a correlation between icequake activity or wavefield anatomy and seismic velocity change estimates. We conclude that the preprocessing of CCFs, especially the removal of segments containing large-amplitude transients, resulted in a sufficiently randomised coda wavefield in the 8-20 s analysis window and thus unbiased dv/v estimates (Hillers et al., 2015). Ballistic components with a dominant ∼N-S propagation direction in summer associated with the icequake activity did not govern the results. We conclude that the obtained change in the elastic properties of the medium are genuine and most likely driven by changes in temperature.

Therefore, we consider the SPITS continuous array data as an important resource to study the behaviour of the permafrost layer in response to the globally increasing temperature associated with climate change. We demonstrated the ability to study the impact of the seasonal temperature variation on permafrost. We also highlight the resolution of a long-term effect that is illustrated by the consistency between the decreasing trend in dv/v and a simultaneous increase in temperatures from 2009 to 2011 observed in the Janssonhaugen borehole (Fig. 9). This type of analysis would benefit from ambient seismic noise measurements within shallower surface layers, requiring the installation of additional sensors with reduced interstation distances. Such a network could be accommodated readily within the aperture limits of the current array, where essential infrastructure in terms of cables and communication lines is already provided. Independent laboratory analysis of Adventdalen permafrost samples also would be of great interest to better quantify the effect of ice saturation on the observed seismic velocity variations (e.g., Zimmerman and Michael, 1986).

Conclusions

Most of the challenges in the application of geophysical investigations in polar environments are related to extreme seasonal changes as well as the permafrost cover (Kneisel et al., 2008). On the one hand, these climate conditions induce large variations in the elastic properties of the ground, allowing for testing of new methodologies in these natural laboratories. On the other hand, the deployment of monitoring systems is hampered by these environmental settings. The installation of a seismic monitoring network within the Adventdalen valley is challenging. First, the long duration of the winter period with snow and ice coverage means that there is only a limited time window available which deployment and maintenance of instruments is feasible. Second, options for instrument installations are limited, which in turn may result in a network geometry that is not optimal for a specific research target. For example, the SEISVAL broadband seismometers could not be installed on the valley plain, but had to be placed on its north and south sides, since a broad braided river emerges during summertime. It is unknown in which seismic frequency range this braided river contributes to the ambient seismic noise field. Only few rock outcrops were available onto which seismometers could be cemented and these boulders are not connected to the bedrock, which increases the possibility of low quality records. The stiffness of the frozen ground prevented burial of the seismometers to shield them from wind. Although the construction of a permanent network such as

SPITS is costly and challenging, it is essential for proper long-term seismic monitoring of geological features such as permafrost. In particular, the array geometry allows for an enhanced signal-to-noise ratio employing array analysis approaches. The deployment of temporary seismic networks is essential as well, since their geometry and thus sensitivity can be adapted to a specific target. In addition, they complement the permanent station coverage. This study demonstrates that passive seismic data acquired over an extended period of time and collected for initially different purposes can be used for environmental applications, such as monitoring the temporal evolution of shallow permafrost layers and thus help to assess its vulnerability to climate change.

Our study emphasises the necessity of combining different monitoring and analysis methods. The results from the various approaches demonstrate the feasibility of geophysical methods for continuous permafrost monitoring. The observations provide suggestions for future seismological investigations and highlight the sensitivities and resolution capabilities of the employed methods. We demonstrated that seismic interferometry applied to several years of continuous data can resolve permafrost dynamics. Specifically, we recovered both seasonal and long-term temperature effects on the permafrost through the measurement of seismic velocity variations.

The main results of our study are:

- A shallow S-wave velocity model of the subsurface representative of late summer conditions was built from active seismic data. The model is characterized by low shear-wave velocities of only 200 m/s within the upper 50 m, increasing to approximately 450 m/s at 100 m depth.

- The temporary SEISVAL network and the permanent SPITS array are suitable for detection and identification of local microseismic events. Detected seismicity consists of icequakes and probably mining-induced events.

- Spectral analysis of the ambient seismic noise recorded at SPITS shows that the energy is dominated by the secondary microseism peak. A stable noise source also is recovered at 0.5-4 Hz.

- An $f - k$ analysis performed on five years of SPITS data (2009-2013) shows that energy corresponding to typical P- and S-wave slownesses dominates over all frequency ranges. Interestingly, this pattern seems to be a temporally stable feature throughout each year, reduced in visibility only during summer months when surface wave velocities prevail.

- This transition between wave types occurs very suddenly, coinciding with the average air temperature exceeding the freezing point and is accompanied by a change in wavefield direction.

- The cross-correlation functions computed between SEISVAL stations was successfully modelled based on a 3-D velocity model of the Adventdalen valley.

- The wavefield observed in the modelled Green's functions fits Rayleigh waves propagating along the length of Adventdalen.

- Seasonal changes in seismic velocity extracted from SPITS array data appear to be correlated with temperature variations in the permafrost below the active layer.

- A decreasing trend in seismic velocity is interpreted as the effect of an increase in the average temperature recorded at Svalbard between 2009 and 2011.

Data and Resources

NORSAR bulletins are available from https://www.norsar.no/seismic-bulletins/. The 12 seismic stations for the SEISVAL experiment were rented from the French national pool of portable seismic instruments Sismob-RESIF (`https://sismob.resif.fr/`). We used a high-performance Python code developed at ISTerre, U. Grenoble-Alpes, to compute the noise correlation functions (Boué et al., 2013; Boué et al., 2014). The 3-D Adventdalen velocity model was updated by systematic gathering of all existing data and their evaluation using the OpendTect freeware (`https://dgbes.com/index.php/software/free#opendtect`) as platform. The open-source sw4 code is available at `https://github.com/geodynamics/sw4`. A part of the plots was made using the Generic Mapping Tools version 6.1.1 (Wessel and Smith, 1998). Supplementary material including additional figures is available to the reader.

Acknowledgments

This work was financed by the Research Council of Norway grant no. 224880 (SafeCO$_2$-II project). The project was sponsored additionally by industry partners Lundin, RWE DEA Norge and Statoil (now Equinor). The first version of the 3-D Adventdalen velocity model was developed in a previous project, likewise funded by the Research Council of Norway (grant no. 189994, SafeCO$_2$ project) and industry partners Lundin, Octio, READ, ConocoPhillips and Statoil (now Equinor). Further, we would like to thank the Norwegian Metacenter for Computational Science (NOTUR) for granting us computation time on their supercomputer Abel to compute 3-D waveform propagation within Adventdalen (SynthCO$_2$ project). We offer our heartfelt thanks to the Longyearbyen CO$_2$ Lab managed by the UNIS CO$_2$ Lab AS for help and support provided throughout the years. We thank K. Isaksen for giving us access to borehole temperature data, S. Sikora, G. Sauvin, P. Zhao, N. Skøyen and P. Lavadera Lubrano for their help on the field, F. Brenguier, M. Campillo, A. Köhler, M. Roth and J. Schweitzer for helpful discussions related to this study, L. Zühlsdorff and E.V. Bergfjord for translating the Adventdalen reservoir model into a NORSAR3D velocity model as well as V. Oye for participation in and active support of the project and review of the manuscript. The authors are thankful to the guest editors M. Pirli and

P. Voss as well as two anonymous reviewers who provided comments that greatly improved the manuscript.

References

Anisimov, O. A. (2007). Potential feedback of thawing permafrost to the global climate system through methane emission, *Environ. Res. Lett.* **2**(4) 045016 7pp.

Bælum, K., Johansen, T., Johnsen, H., Rød, K., Ruud, B. O., and A. Braathen (2012). Subsurface structures of the Longyearbyen CO_2 Lab study area in Central Spitsbergen (Arctic Norway), as mapped by reflection seismic data, *Norw. J. Geol.* **92**(4) 377-389.

Bergh, S. G., Braathen, A., and A. Andresen (1997). Interaction of basement-involved and thin-skinned tectonism in the tertiary fold-thrust belt of central Spitsbergen, Svalbard, *AAPG Bull.* **81**(4) 637-661.

Boore, D., and M. Nafi Toksöz (1969). Rayleigh wave particle motion and crustal structure, *Bull. Seismol. Soc. Am.* **9**(1) 331-346.

Boué, P., Poli, P., Campillo, M., Pedersen, H., Briand, X., and P. Roux (2013). Teleseismic correlations of ambient seismic noise for deep global imaging of the Earth, *Geophys. J. Int.* **194** 844-848.

Boué, P., Roux, P., Campillo, M., and X. Briand (2014). Phase velocity tomography of surface waves using ambient noise cross correlation and array processing, *J. Geophys. Res. Solid Earth* **119**(1) 519-529.

Braathen, A., Bælum, K., Christiansen, H. H., Dahl, T., Eiken, O., Elvebakk, H., Hansen, F., Hanssen, T. H., Jochmann, M., Johansen, T. A., Johnsen, H., Larsen, L., Lie, T., Mertes, J., Mørk, A., Mørk, M. B., Nemec, W., Olaussen, S., Oye, V., Rød, K., Titlestad, G. O., Tveranger, J., and K. Vagle (2012). The Longyearbyen CO_2 Lab of Svalbard, Norway - initial assessment of the geological conditions for CO_2 sequestration, *Norw. J. Geol.* **92**(4) 353-376.

Brenguier, F., Shapiro, N. M., Campillo, M., Ferrazzini, V., Duputel, Z., Coutant, O., and A. Nercessian (2008). Towards forecasting volcanic eruptions using seismic noise, *Nat. Geosci.* **1**(2) 126-130.

Bungum, H., Alsaker, A., Kvamme, L. B., and R. A. Hansen (1991). Seismicity and seismotectonics of Norway and nearby continental shelf areas, *J. Geophys. Res. Solid Earth* **96**(B2) 2249-2265.

Christiansen, H., Etzelmüller, B., Isaksen, K., Juliussen, H., Farbrot, H., Humlum, O., Johansson, M., Ingeman-Nielsen, T., Kristensen, L., Hjort, J., Holmlund, P., Sannel, A., Sigsgaard, C., Åkerman, H., Foged, N., Blikra, L., Pernosky, M., and R. Ødegård (2010). The thermal state of permafrost in the Nordic area during the International Polar Year 2007–2009, *Permafrost and Periglacial Process.* **21**(2) 156-181.

Colombi, A., Chaput, J., Brenguier, F., Hillers, G., Roux, P., and M. Campillo (2014). On the temporal stability of the coda of ambient noise correlations, *C. R. Geosci.* **346** 307-316.

Crawford, J. M., Doty, W. E. N., and M. R. Lee (1960). Continuous signal seismograph, *Geophysics* **25**(1) 95-105.

Demuth, A., Ottemöller, L., and H. Keers (2016). Ambient noise levels and detection threshold in Norway, *J. Seismol.* **20**(3) 889-904.

Dou, S. and J. B. Ajo-Franklin (2014). Full-wavefield inversion of surface waves for mapping embedded low-velocity zones in permafrost, *Geophysics*, **79**(6) EN107-EN124.

Dou, S., Nakagawa, S., Dreger, D., and J. Ajo-Franklin (2016). A rock-physics investigation of unconsolidated saline permafrost: P-wave properties from laboratory ultrasonic measurements, *Geophysics* **81**(1) WA233-WA245.

Eisner, L. and R. W. Clayton (2001). A reciprocity method for multiple-source simulations, *Bull. Seism. Soc. Am.* **91**(3) 553-560.

Hadziioannou, C., Larose, E., Coutant, O., Roux, P., and M. Campillo (2009). Stability of monitoring weak changes in multiply scattering media with ambient noise correlation: Laboratory experiments, *J. Acoust. Soc. Am.* **125**(6) 3688-3695.

Harris, D., Albaric, J., Goertz-Allmann, B., Kühn, D., Sikora, S., and V. Oye (2017). Interference suppression by adaptive cancellation in a high arctic seismic experiment, *Geophysics* **82**(4) V201-V209.

Hillers, G., Ben-Zion, Y., Campillo, M., and D. Zigone (2015). Seasonal variations of seismic velocities in the San Jacinto fault area observed with ambient seismic noise, *Geophys. J. Int.* **202**(2) 920-932.

Humlum, O., Instanes, A., and J. Sollid (2003). Permafrost in Svalbard: a review of research history, climatic background and engineering challenges, *Polar Res.* **22**(2) 191-215.

Isaksen, K., Holmlund, P., Sollid, J. L., and C. Harris (2001). Three deep Alpine-permafrost boreholes in Svalbard and Scandinavia, *Permafrost and Periglacial Process.* **12**(1) 13-25.

Isaksen, K., Sollid, J. L., Holmlund, P., and C. Harris (2007). Recent warming of mountain permafrost in Svalbard and Scandinavia, *J. Geophys. Res. Earth Surf.* **112** F02S04.

James, S. R., Knox, H. A., Abbott, R. E., Panning, M. P., and E. J. Screaton (2019). Insights into permafrost and seasonal active-layer dynamics from ambient seismic noise monitoring, *J. Geophys. Res. Earth Surf.* **124**(7) 1798-1816.

James, S. R., Knox, H. A., Abbott, R. E., and E. J. Screaton (2017). Improved moving window cross-spectral analysis for resolving large temporal seismic velocity changes in permafrost, *Geophys. Res. Lett.* **44**(9) 4018-4026.

Kneisel, C., Hauck, C., Fortier, R., and B. Moorman (2008). Advances in geophysical methods for permafrost investigations, *Permafrost and Periglacial Process.* **19**(2) 157-178.

Köhler, A., Chapuis, A., Nuth, C., Kohler, J., and C. Weidle (2012). Autonomous detection of calving-related seismicity at Kronebreen, Svalbard, *Cryosphere* **6** 393-406.

Köhler, A., Nuth, C., Schweitzer, J., Weidle, C., and S. J. Gibbons (2015). Regional passive seismic monitoring reveals dynamic glacier activity on Spitsbergen, Svalbard, *Polar Res.* **34**(1) 26178.

Köhler, A., and C. Weidle (2019). Potentials and pitfalls of permafrost active layer monitoring using the HVSR method: a case study in Svalbard, *Earth Surf. Dyn.* **7**(1) 1-16.

Krim, H., and M. Viberg (1996). Two decades of array signal processing research: the parametric approach, *IEEE Signal Process. Mag.* **13**(4) 67-94.

Kühn, D., Oye, V., Albaric, J., Harris, D., Hillers, G., Braathen, A., and S. Olaussen (2014). Preparing for CO_2 storage in the Arctic – Assessing background seismic activity and noise characteristics at the CO_2 Lab site, Svalbard, *Energy Procedia* **63** 4313-4322.

Kula, D., Olszewska, D., Dobiński, W., and M. Glazer (2018). Horizontal-to-vertical spectral ratio variability in the presence of permafrost, *Geophys. J. Int.* **214**(1) 219-231.

Kværna, T., and F. Ringdahl (1986). Stability of various f-k estimation techniques, *NORSAR Semiannual Tech. Summary* **1-86/87** 29-40. http://doi.org/10.21348/p.1986.0001.

LeBlanc, A., Fortier, R., Allard, M., Cosma, C., and S. Buteau (2004). Seismic cone penetration test and seismic tomography in permafrost, *Can. Geotech. J.* **41**(5) 796-813.

Lehujeur, M., Vergne, J., Schmittbuhl, J., Zigone, D., Le Chenadec, A., and E. Team (2018). Reservoir imaging using ambient noise correlation from a dense seismic network, *J. Geophys. Res. Solid Earth* **123**(8) 6671-6686.

Lobkis, O., and R. Weaver (2001). On the emergence of the Green's function in the correlations of a diffuse field, *J. Acoust. Soc. Am.* **110**(6) 3011-3017.

Lubrano Lavadera, P., Kühn, D., Dando, B., Lecomte, I., Senger, K., and Å. Drottning (2018). CO_2 storage in the high Arctic: efficient modelling of pre-stack depth-migrated seismic sections for survey planning, *Geophys. Prospect.* **66**(6) 1180-1200.

McNamara, D., Hutt, C., Gee, L., Benz, H. M., and R. Buland (2009). A method to establish seismic noise baselines for automated station assessment, *Seismol. Res. Lett.* **80**(4) 628-637.

Mykkeltveit, S., Dahle, A., Fyen, J., Kværna, T., Larsen, P., Paulsen, R., Ringdal, F., and I. K. Bungum (1992). Extensions of the Northern Europe Regional Array Network - new small-aperture arrays at Apatity, Russia, and on the Arctic island of Spitsbergen, *NORSAR Semiannual Tech. Summary* **I-92/93** 58-71. http://doi.org/10.21348/p.1992.0001.

Neidell, N., and M. Taner (1971). Semblance and other coherency measures for multichannel data, *Geophysics* **36**(3) 482-497.

NORSAR (1971). NORSAR Seismic Bulletins. http://doi.org/10.21348/b.0001.

Olaussen, S., Senger, K., Braathen, A., Grundvåg, S., and A. Mørk (2019). You learn as long as you drill; research synthesis from the Longyearbyen CO_2 Laboratory, Svalbard, Norway, *Norw. J. Geol.* **99** 157-181.

Oye, V., Braathen, A., and U. Polom (2013). Preparing for CO_2 storage at the Longyearbyen CO_2 Lab: microseismic monitoring of injection tests, *First Break* **31** 95-101.

Oye, V., Gharti, H., Kühn, D., and A. Braathen (2010). Microseismic monitoring of fluid injection at the Longyearbyen CO_2 Lab, Svalbard, *Cahiers du Centre européen de géodynamique et de séismologie* **30** 109-114.

Petersen, J. (1993). Observations and modeling of seismic background noise, *Open-File Report, US Geological Survey, Albuquerque, NM* **93-322** 42pp.

Petersson, N. A. and B. Sjögreen (2015). Wave propagation in anisotropic elastic materials and curvilinear coordinates using a summation-by-parts finite difference method, *J. Comput. Phys.* **299** 820–841.

Petersson, N. A. and B. Sjögreen (2017). User's guide to SW4, version 2.0. *Lawrence Livermore National Laboratory* Tech. Report **LLNL-SM-741439**

Pirli, M. (2003). Norsar system responses manual, 3rd ed, *NORSAR Tech. Report* 304pp. http://doi.org/10.21348/p.2013.0001.

Pirli, M., Schweitzer, J., and B. Paulsen (2013). The Storfjorden, Svalbard, 2008–2012 aftershock sequence: seismotectonics in a polar environment, *Tectonophysics* **601** 192-205.

Polom, U. (2006). Vibration generator for seismic applications, US Patent 7136325b2.

Polom, U., Druivenga, G., Grossmann, E., Grüneberg, S., and W. Rode (2011). Transportabler Scherwellenvibrator: Deutsches Patent und Markenamt, *Patentschrift DE10327757B4*.

Polom, U., Hansen, L., Sauvin, G., L'Heureux, J.-S., Lecomte, I., Krawczyk, C. M., Vanneste, M., and O. Longva (2010). High-resolution SH-wave seismic reflection for characterization of onshore ground conditions in the Trondheim harbor, Central Norway, in *Advances in Near-surface Seis-*

mology and Ground-penetrating Radar, Geophysical Developments Series, SEG Tulsa 297-312.

Poupinet, G., Ellsworth, W. L., and J. Frechet (1984). Monitoring velocity variations in the crust using earthquake doublets: An application to the Calaveras Fault, California, *J. Geophys. Res. Solid Earth* **89**(B7) 5719-5731.

Raup, B., Racoviteanu, A., Khalsa, S., Helm, C., Armstrong, R., and Y. Arnaud (2007). The GLIMS geospatial glacier database: a new tool for studying glacier change, *Global Planet. Change* **56** 101-110.

Rost, S., and C. Thomas (2002). Array seismology: Methods and applications, *Rev. Geophys.* **40**(3) 2–1 - 2–27.

Roux, P., Wathelet, M., and A. Roueff (2011). The San Andreas Fault revisited through seismic-noise and surface-wave tomography, *Geophys. Res. Lett.* **38**(13) L13319.

Schaefer, K., Lantuit, H., Romanovsky, V. E., Schuur, E. A. G., and R. Witt (2014). The impact of the permafrost carbon feedback on global climate, *Environ. Res. Lett.* **9**(8) 085003.

Schweitzer, J., Köhler, A., and J. M. Christensen (2021). Development of the NORSAR network over the last 50 years, *Seismol. Res. Lett.* http://doi.org/10.1785/0220200375.

Seneviratne, S., Donat, M., Pitman, A., Knutti, R., and R. L. Wilby (2016). Allowable CO_2 emissions based on regional and impact-related climate targets, *Nature* **529** 477–483.

Senger, K., Tveranger, J., Braathen, A., Olaussen, S., Ogata, K., and L. Larsen (2014). CO_2 storage resource estimates in unconventional reservoirs: insights from a pilot-sized storage site in Svalbard, Arctic Norway, *Environ. Earth Sci.* **73**(8) 3987-4009.

Sens-Schönfelder, C., and U. Wegler (2006). Passive image interferometry and seasonal variations of seismic velocities at Merapi Volcano, Indonesia, *Geophys. Res. Lett.* **33**(21) L21302.

Shapiro, N. M., and M. Campillo (2004). Emergence of broadband Rayleigh waves from correlations of the ambient seismic noise, *Geophys. Res. Lett.* **31**(7) L07614.

Shapiro, N. M., Campillo, M., Stehly, L., and M. H. Ritzwoller (2005). High-resolution surface-wave tomography from ambient seismic noise, *Science* **307**(5715) 1615-1618.

Sjögreen, B. and N. A. Petersson (2012). A fourth order accurate finite difference scheme for the elastic wave equation in second order formulation, *J. Sci. Comput.* **52**(1) 17-48.

Snieder, R. (2004). Extracting the Green's function from the correlation of coda waves: a derivation based on stationary phase, *Phys. Rev. E* **69**(4) 046610.

Snieder, R., Grêt, A., Douma, H., and J. Scales (2002). Coda wave interferometry for estimating nonlinear behavior in seismic velocity, *Science* **295**(5563) 2253-2255.

Stehly, L., Campillo, M., and N. Shapiro (2006). A study of the seismic noise from its long-range correlation properties, *J. Geophys. Res. Solid Earth* **111** B10306.

Stemland, H. M., Johansen, T., and B.O. Ruud (2020). Potential Use of Time-Lapse Surface Seismics for Monitoring Thawing of the Terrestrial Arctic, *Appl. Sci.* **10**(5) 1875.

Timur, A. (1968). Velocity of compressional waves in porous media at permafrost temperatures, *Geophysics* **33**(4) 584-595.

Tsai, V. (2010). The relationship between noise correlation and the Green's function in the presence of degeneracy and the absence of equipartition, *Geophys. J. Int.* **182**(3) 1509-1514.

Wessel, P. and W. H. F. Smith (1998). New, improved version of generic mapping tools released, *Eos Trans. AGU* **79** 579-579.

Westermann, S., Wollschläger, U., and J. Boike (2010). Monitoring of active layer dynamics at a permafrost site on Svalbard using multi-channel ground-penetrating radar, *The Cryosphere* **4**(4) 475-487.

Williams, P., and M. Smith (1989). *The Frozen Earth: Fundamentals of Geocryology*, Cambridge University Press.

Zimmerman, R. W., and S. K. Michael (1986). The effect of the extent of freezing on seismic velocities in unconsolidated permafrost, *Geophysics* **51**(6) 1285–1290.

Full mailing address for each author

Julie Albaric: Laboratoire Chrono-environnement, University of Franche-Comté, 16 route de Gray, 25030 Besançon, France.

Daniela Kühn: Applied Seismology, NORSAR, Gunnar Randers vei 15, N-2007 Kjeller, Norway.

Matthias Ohrnberger: Institute of Geosciences, University of Potsdam, Campus Golm Building 27, Am Neuen Palais 10, 14469 Potsdam, Germany.

Nadege Langet: Applied Seismology, NORSAR, Gunnar Randers vei 15, N-2007 Kjeller, Norway.

Dave Harris: Deschutes Signal Processing LLC, 81211 E Wapinitia Rd Maupin, OR 97037, Maupin, Oregon, USA.

Ulrich Polom: Leibniz Institute for Applied Physics, Stilleweg 2, 30655 Hannover, Germany.

Isabelle Lecomte: Department of Earth Science, University of Bergen, Postboks 7803, NO-5020 Bergen, Norway.

Gregor Hillers: Institute of Seismology, University of Helsinki, PO BOX 68, 00014 Helsinki, Finland.

List of Figures

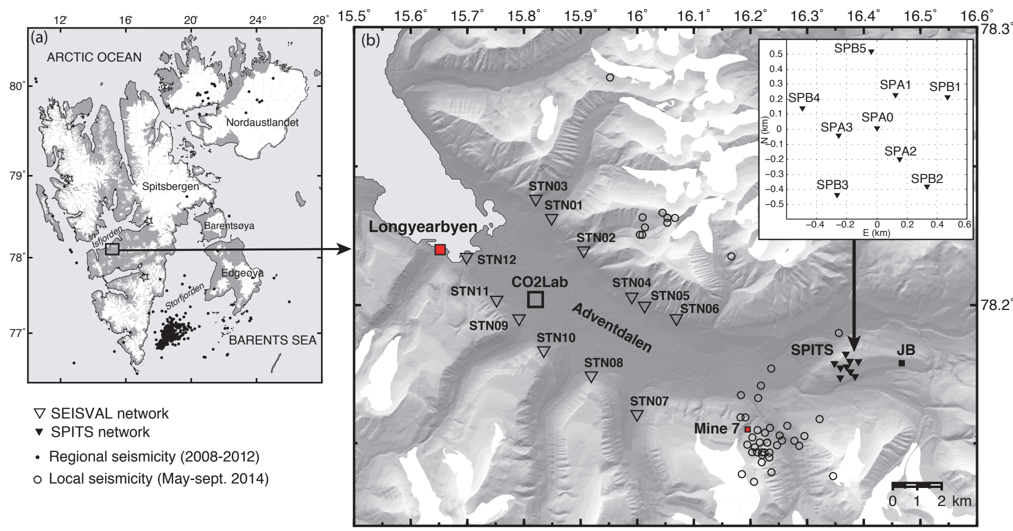

Figure 1: Overview on the study area. (a) Map of the Svalbard Archipelago. (b) Map of the Adventdalen area. The location of the CO_2 Lab is indicated by an open square. The SEISVAL seismic network and the SPITS array are indicated by open and black filled triangles, respectively. The names and relative locations of the SPITS array stations are indicated in the upper right corner inset. Black filled circles in (a) correspond to regional seismicity between 2008 and 2018 (Pirli et al., 2013) and empty circles in (b) to local events located in this study. White areas correspond to glaciers (mapped using data from `http://www.glims.org` (Raup et al., 2007)). JB refers to the Janssonhaugen temperature borehole (Isaksen et al., 2001).

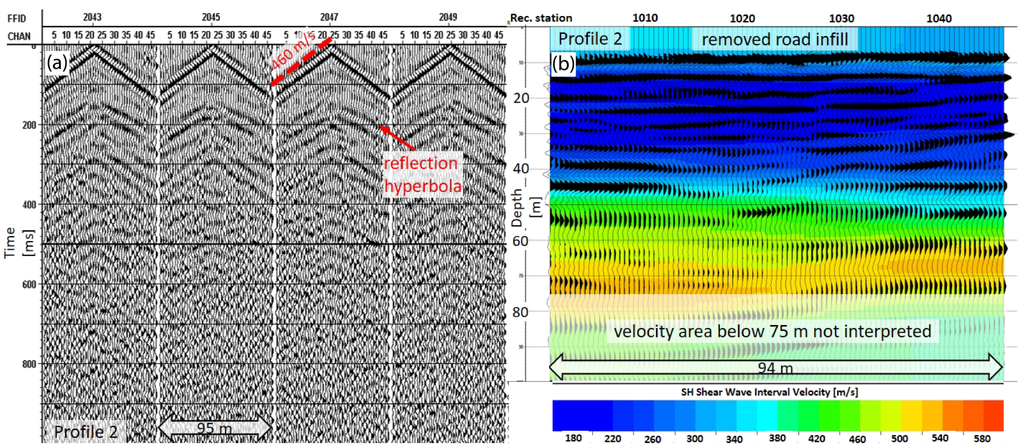

Figure 2: Profile 2 along the main road. (a) Examples of shot records. (b) Final depth-converted finite-difference-migrated time section, with superimposed colour-coded S-wave interval velocities.

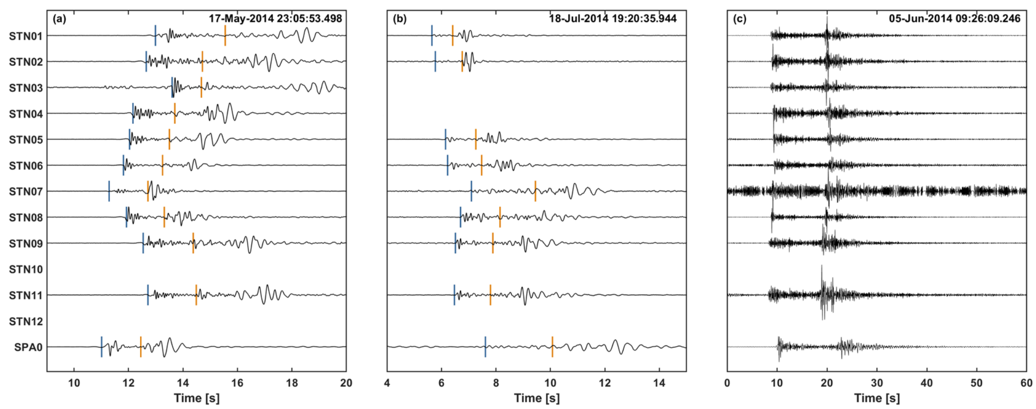

Figure 3: Vertical component records of (a) a local event located to the south-east with respect to the SEISVAL network; (b) a local event located to the north with respect to the SEISVAL network and (c) a regional earthquake. Data are filtered between 2-20 Hz. In (a) and (b), the blue and orange bars represent the P- and S-wave picks used for event location.

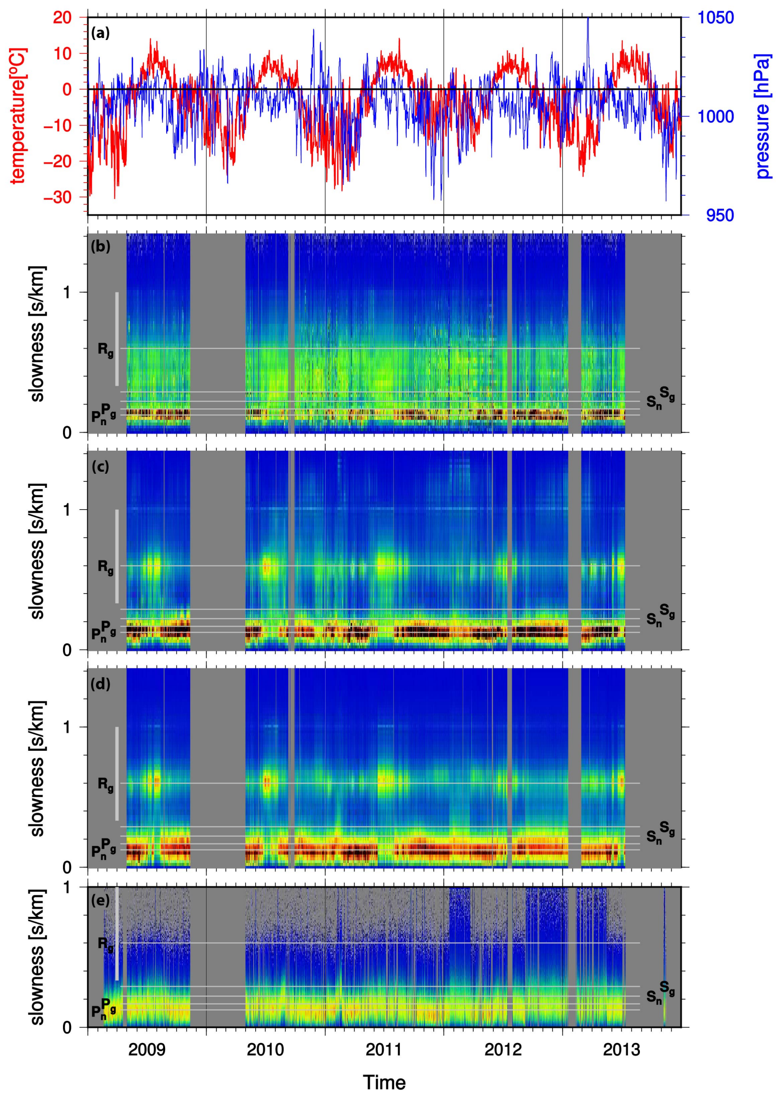

Figure 4: (a) Temperature and air pressure are compared to absolute horizontal slowness from 2009-2013 for frequencies: (b) 6-18 Hz, (c) 3-9 Hz, (d) 1.5-4.5 Hz, and (e) 0.5-2.0 Hz. Horizontal slowness is presented as histograms for 3-hour intervals. Colour scales are relative and not comparable given choice of window lengths for different frequency bands. Horizontal grey lines mark standard slowness values for local body wave phases ($P_g \approx 1/6$ s/km, $P_n \approx 1/8$ s/km, $S_g \approx 1/3.5$ s/km, $S_n \approx 1/4.5$ s/km, $R_g \approx 1/1.6$ s/km).

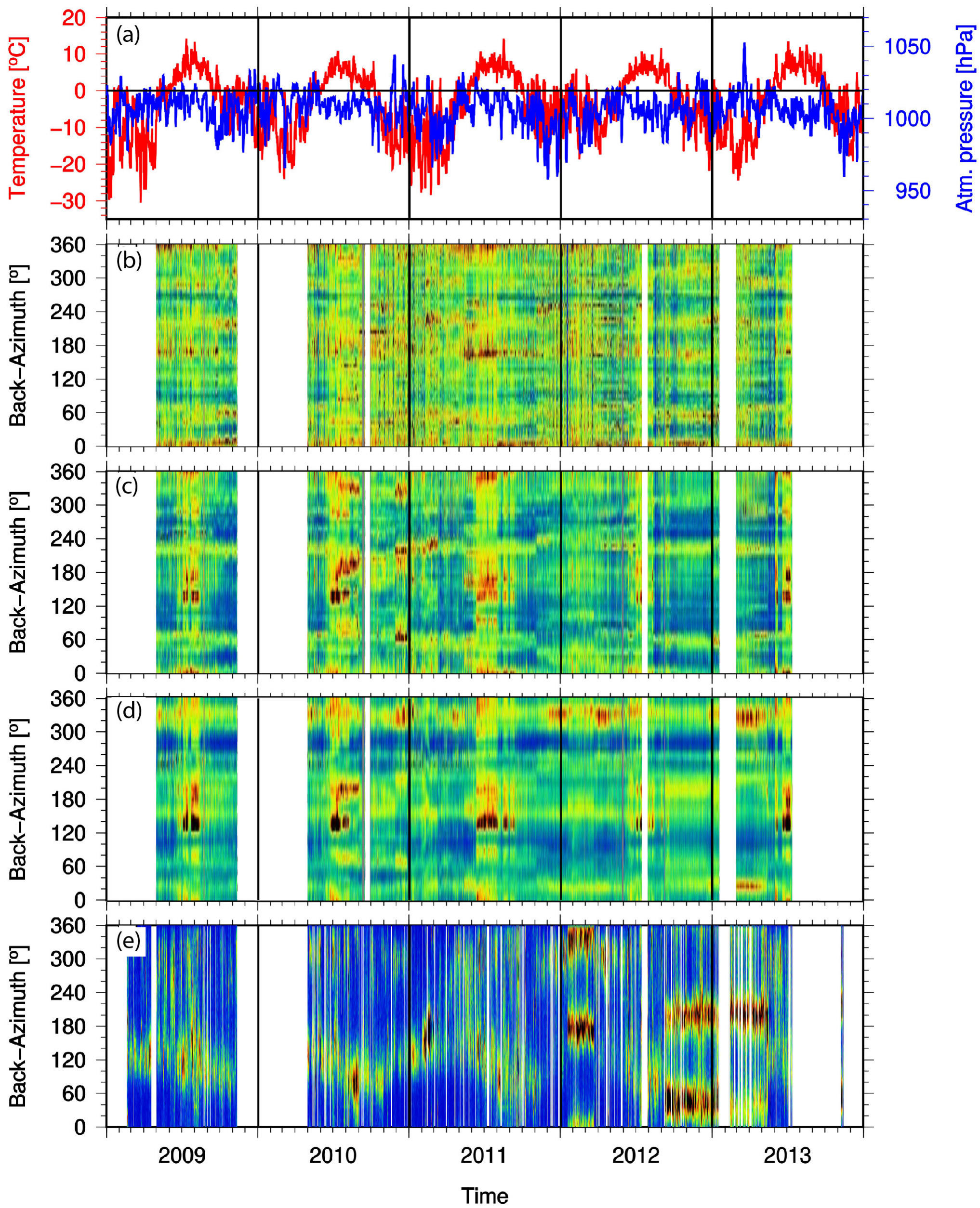

Figure 5: (a) Temperature and air pressure are compared from 2009-2013 to backazimuths computed for absolute horizontal slowness filtered in the slowness range from 0.33 s/km to 1 s/km for frequencies: (b) 6-18 Hz, (c) 3-9 Hz, (d) 1.5-4.5 Hz, and (e) 0.5-2.0 Hz. Colour scales are relative and not comparable given choice of window lengths for different frequency bands.

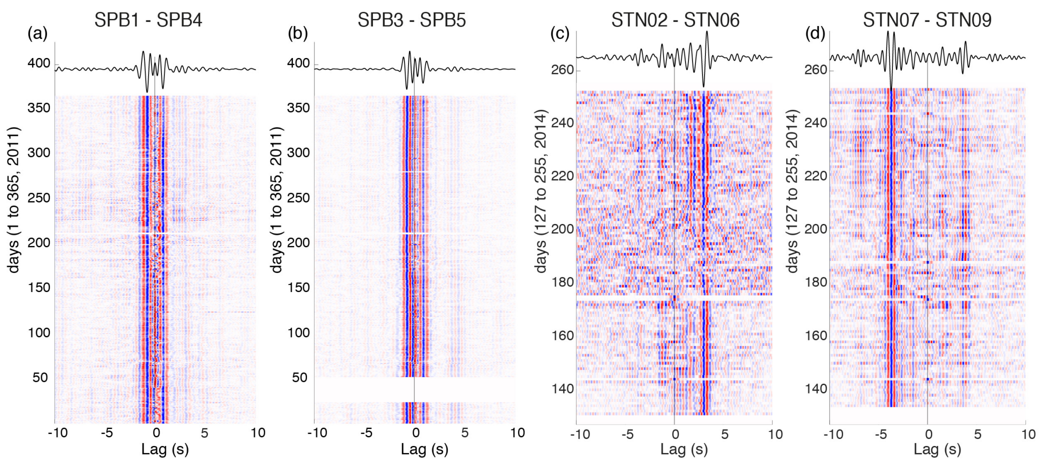

Figure 6: Examples of cross-correlation functions computed from SPITS and SEISVAL data (vertical components) for stations pairs: (a) SPB1-SPB4 (N-S direction), (b) SPB3-SPB5 (E-W direction) (c) STN02-STN06 (NW-SE direction, north side of Adventdalen), (d) STN07-STN09 (SE-NW direction, south side of Adventdalen).

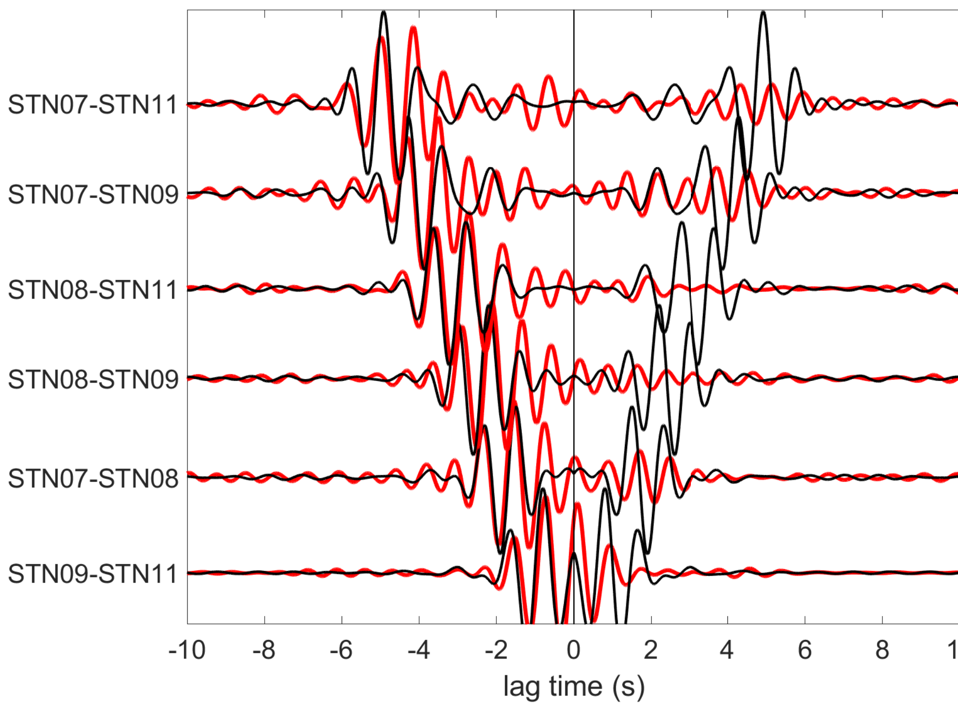

Figure 7: Comparison of modelled Green's functions and recorded cross-correlation functions for sensor pairs on the south side of Adventdalen; black lines: modelled Green's functions, red lines: measured cross-correlation stacks; both data filtered within 0.75-1.5 Hz.

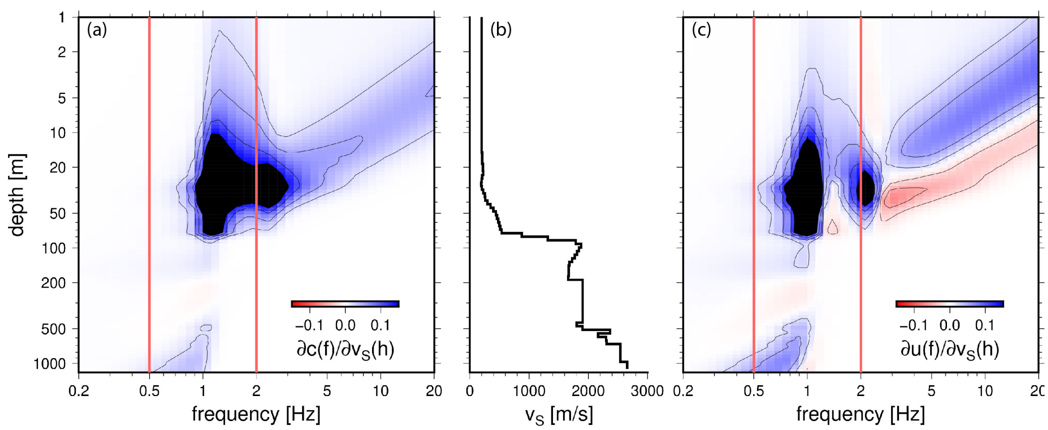

Figure 8: Sensitivity of Rayleigh wave phase (a) and group (c) velocity to changes in shear wave velocity with depth for 1-D velocity model (b) including measured shallow shear wave velocities; red vertical lines in (a) and (c) mark 0.5-2 Hz frequency band for which velocity variations were observed in the following. Please note logarithmic scale of axes.

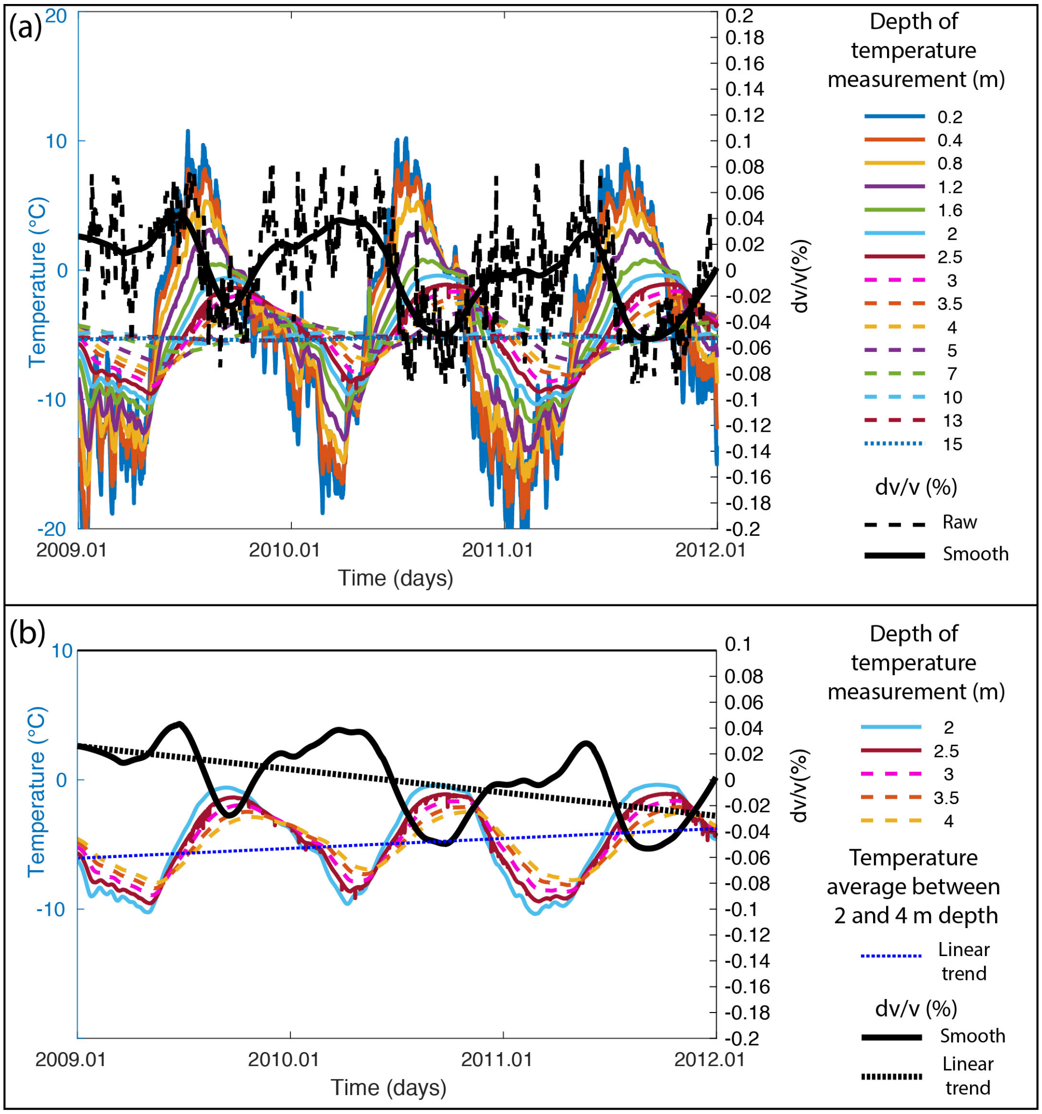

Figure 9: Relative seismic velocity changes compared with ground temperatures. Black solid line represents locally weighted linear regression of dv/v estimated with the doublet method for the frequency range 0.5-2 Hz (represented as black dashed line); coloured curves represent borehole temperatures measured at different depths (0.2 to 15 m) within a borehole at Janssonhaugen (denoted JB on Fig. 1; Isaksen et al., 2001, 2007). (a) Temperature from 0.2 to 15 m depth plotted together with dv/v (raw and smoothed curves); (b) temperature from 2 to 4 m depth, smoothed dv/v and linear velocity and temperature trends computed from the smoothed dv/v curve and temperature averaged between 2 and 4 m depth, respectively.

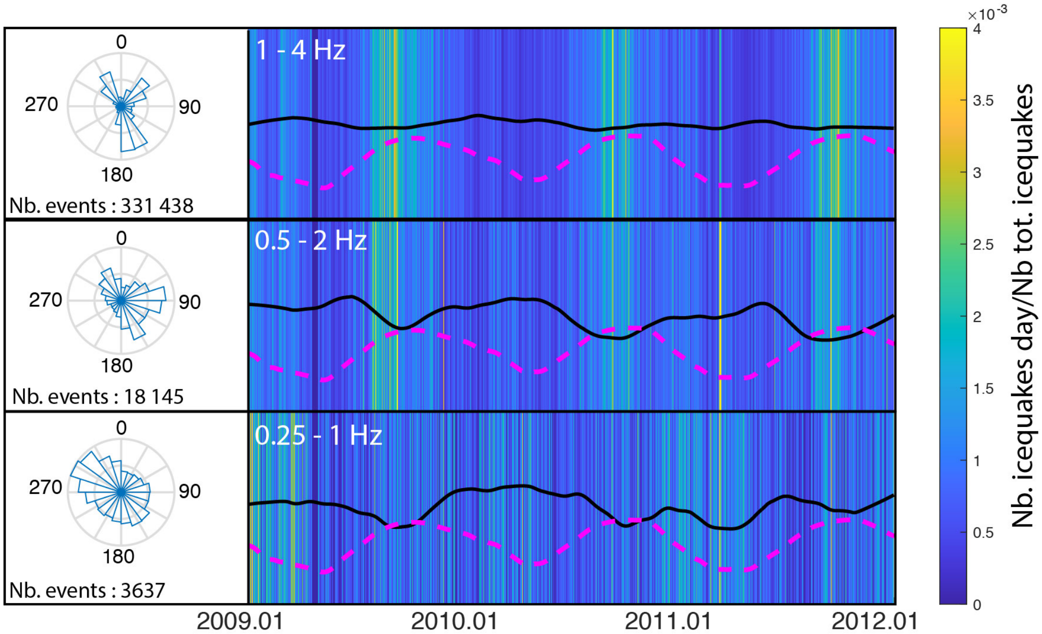

Figure 10: Left: rose plots indicating azimuthal distributions of events according to their dominant frequency for the years 2009 to 2011. The absolute number of detected events in each frequency range is indicated below each rose plot. Right: number of high frequency events (icequakes) per day normalised over the whole time period (see colour bar) compared to dv/v estimates (black lines) and temperature measured at 3 m depth variations (magenta dashed lines). From top to bottom: frequency ranges of 1-4 Hz, 0.5-2 Hz and 0.25-1 Hz.